Morphogenesis of the diamond-type stereom microlattice and the origin of saddle-shaped minimal surfaces in the echinoderm skeleton

Kamil Humański[a], Giulio Facchini[b], Jenifer Croce[c], Dorota Kołbuk[d], Philippe Dubois[e], Przemysław Gorzelak[a]*

This manuscript is currently under consideration at Acta Biomaterialia (Elsevier).

[a]Institute of Paleobiology, Polish Academy of Sciences, Warszawa, Poland

[b]Laboratoire Matière et Systèmes Complexes, CNRS, Université Paris Cité, Paris, France

[c]Laboratoire de Biologie du Développement de Villefranche-sur-Mer (LBDV), Institut de la Mer de Villefranche (IMEV), Sorbonne Université, CNRS, Villefranche-sur-Mer, France

[d]UCD Earth Institute and School of Biology and Environmental Science, University College Dublin, Belfield, Dublin, Ireland

[e]Laboratoire de Biologie Marine, Faculté des Sciences, Université Libre de Bruxelles, Bruxelles, Belgium

*Corresponding author: pgorzelak@twarda.pan.pl (P. Gorzelak)

Abstract

Echinoderm endoskeleton has a unique trabecular microstructure known as stereom, which can exhibit highly ordered geometries. A particularly striking example of these geometries is the recently discovered "diamond-type" stereom, characterized by a diamond triply periodic minimal surface (D-TPMS) geometry and distinguished by its exceptional mechanical and structural properties. Despite its promising features for engineering applications, the morphogenesis of this microarchitecture remains poorly understood, notably due to its

uniqueness in the natural world. Here, we applied a multimodal imaging and labeling approach to investigate the developmental processes underlying the formation of the diamond-type stereom in adults of a starfish species *Protoreaster nodosus*. We showed that this stereom type develops through two principal marginal growth patterns: trabecular trifurcation, which generates successive, horizontally spreading layers and occurs on flat external plate surfaces oriented approximately along the crystallographic {111} planes of the D-TPMS; and trabecular bifurcation, typically occurring along the edges of external plates and in the regions between trifurcating zones, aligned with the crystallographic {100} planes of the D-TPMS lattice. Although these growth patterns may proceed at different rates, they are tightly coordinated, resulting in the coherent D-TPMS microarchitecture. Furthermore, we demonstrated that F-actin cytoskeletal activity is consistently associated with active biomineralization fronts (trabecular tips), regardless of whether the stereom is of the diamond-type or of a less ordered, galleried form. Notably, we also observed that the formation of lateral bridges between adjacent stereom trabeculae is often preceded by the appearance of catenoid-like F-actin structures, suggesting a guiding and templating role for the cytoskeleton in building trabecular connectivity and shaping its peculiar curvature profile. Given the structural conservation of saddle-like features across multiple stereom types, we hypothesize that such minimal surface geometries may emerge as a result of tension-driven cytoskeletal dynamics acting as a physical template during biomineralization. Our observations underscore the critical involvement of the cytoskeleton in adult echinoderm biomineralization, implying that cytoskeletal patterning may actively contribute to complex adult skeletal microarchitecture.

Statement of Significance

Triple periodic minimal surfaces (TPMS) are geometrically regular surfaces that extend periodically in three dimensions and locally minimize surface area by maintaining zero mean curvature. Among different TPMS structures, the diamond-type (D-TPMS) is particularly notable for its exceptional mechanical stability, uniform porosity, and minimal surface area-to-volume ratio. Although TPMS-like microarchitectures are not uncommon in nature, D-TPMS structures, with such exceptionally large lattice parameters (>10 μm), are exceedingly rare. One notable natural example of these is the stereom of certain echinoderms. However, the fundamental question of what governs the formation of such highly ordered microstructures remains unresolved. To investigate this, we applied a multi-modal labeling and imaging approach to elucidate the general principles of diamond-type stereom morphogenesis. This study not only provides the first insights into the growth dynamics of this unique microarchitecture, but also highlights the essential role of the cytoskeleton, particularly F-actin, in guiding trabecular connectivity and the emergence of minimal surface geometry, regardless of whether the stereom is regular (periodic in three dimensions) or not (non-periodic, with a more irregular arrangement of trabeculae).

Key words: D-TPMS, starfish, sea star, biomineralization, F-actin, cytoskeleton.

1. Introduction

Stereom is a unique form of skeletal microstructure, regarded as a synapomorphy of all echinoderms [1]. It is a three-dimensional meshwork of trabeculae that branch and intersect, forming a porous and mechanically robust single-crystal magnesian calcite [2]. Variations in stereom porosity, regularity, and structural directionality have led to the distinction of several stereom types, including rectilinear (trabeculae arranged in a regular cubic or orthorhombic lattice), galleried (parallel trabecular galleries oriented in a single direction), and labyrinthic

(irregular trabecular meshwork), among others [3]. Some of these stereom types have been reported as carrying phylogenetic signals useful for resolving relationships among echinoderm taxa [4]. Furthermore, within the same organism, various stereom types may occur in different skeletal elements or within the same element of a single organism, often reflecting functional specialization of those elements [4-6].

Despite their structural diversity, all stereom types share a common saddle-like profile [4] and display a similar basic developmental pathway [7-11]: their formation begins with the growth of conical protrusions (trabecular tips) that become interconnected through lateral bridging, giving rise to trabecular meshwork. As such, these early structures give rise to a fine meshwork of inner stereom, which may successively thicken and expand at a slow rate through the incremental deposition of biomineral layers. At the cellular level, according to the current model of stereom growth, the elongation of trabeculae is mediated by skeleton-forming cells (referred to as sclerocytes or calcoblasts), which extend thin cytoplasmic processes (skeletal sheaths) that envelop the growing trabecular tips [12, 13]. Between the cytoplasmic processes and the surface of the already deposited biomineral, a confined space occurs in which biomineralization takes place [13, 14].

The conservation of the saddle-shape microstructure in the stereom of all echinoderms suggests that such a special geometry is inherited from a common self-organising morphogenetic process driving structural complexity. Notably, interactions between soft biological tissues and local curvature have been demonstrated in various organisms and across multiple scales, including the cellular level [15], where they appear to be mediated by the cytoskeleton. Accordingly, in echinoderm embryos and larvae, phalloidin-labeling experiments have recently demonstrated that cytoskeleton plays an important role in biomineralization by guiding morphogenesis. In particular, in echinoid embryos it has been shown that F-actin accumulates around the growing larval spicules [16], particularly at their

extending tips [17, 18]. Furthermore, inhibition of F-actin has been shown to induce abnormal, ectopic branching of larval spicules [18]. Recently, F-actin filaments have also been observed connecting pairs of trabeculae in the stereom constituting the sclerites of sea cucumber juveniles (young post-metamorphosis adults), apparently initiating directed growth toward each other, ultimately leading to fusion of opposing trabecular tips [19]. Despite these studies, the role of F-actin in the formation of more complex stereom architectures, particularly within the plates of adult echinoderms, remains largely unexplored. Furthermore, it remains unclear to what extent F-actin is merely a component of a complex skeletogenic machinery, or rather a key determinant of the final curvature profile of the stereom.

In some starfish, sea urchin and sea lily species, the stereom of adults, can exhibit highly organized, regular patterns, such as the recently described "diamond-type" stereom (a specific variant of rectilinear stereom) [20-22]. This structure features a diamond triply periodic minimal surface geometry (D-TPMS) - an exquisitely ordered and periodic surface forming an interconnected diamond-like network, resulting in a highly efficient microarchitecture that is exceptionally rare in nature [23]. It demonstrates high mechanical strength, including remarkable specific energy absorption capabilities [20]. However, the *in vivo* formation mechanisms of these complex and highly periodic microstructures, especially given their large lattice parameters (>10 μm), as well as the involvement of F-actin during these mechanisms, remain unknown. Indeed, although at the nanoscale, the formation and stability of TPMS with lattice parameters up to ~100 nm (observed in certain biological systems, including in butterfly wing scales [24]) can be attributed to self-assembly of soft membranes governed by competing molecular interactions among components like lipids or copolymers [25], the mechanism underlying the emergence of such architectures at the microscopic scale remains puzzling. Understanding the biomineralization processes underlying these

microstructures would however be of great value, not only to biological sciences, but also to the materials science community.

Here, we explored the growth dynamics and morphogenesis of the recently identified diamond-type stereom in the adult starfish species *Protoreaster nodosus*. By integrating complementary staining techniques with imaging approaches, we characterized the development of this highly ordered microarchitecture. To assess the potential involvement of the F-actin cytoskeleton in stereom formation, we further examine the spatial distribution of F-actin filaments, aiming to elucidate their potential role in shaping the stereom microlattice and regulating biomineralization processes. Altogether, these analyses led us to discover that diamond-type stereom develops through two principal marginal growth patterns, and that the cytoskeleton might play an important role in guiding and templating trabecular connectivity, while also shaping its distinctive curvature profile.

2. Materials and methods

2.1. Starfish specimens

The study was conducted at the Laboratory of Marine Biology in Bruxelles (Université Libre de Bruxelles, Belgium) on a commercially available (De Jong Marinelife B.V.) and unprotected wild-type (i.e., not genetically altered) starfish species *Protoreaster nodosus*, in which a diamond-type stereom microstructure was recently discovered [20]. Prior to experiments, a total of 25 small starfish, ca. 2.5-6 cm in arm length, underwent a 2-week acclimatization: they were kept in three aerated, closed-circuit, ca. 100 L aquaria containing natural seawater (salinity ~33.3 psu, temperature ~27°C, pH ~7.95) (see Figure S1, Table S2).

2.2. Scanning Electron Microscopy imaging

Scanning Electron Microscopy (SEM) imaging was performed on two specimens which were not used in any labeling experiments. Those specimens were rinsed in ultra-pure water, dried

149 and dehydrated. Samples were then incubated in 5% sodium hypochlorite solution for one
150 hour. A few samples were also incubated for 30 minutes in a two-fold diluted solution to
151 preserve the connecting tissue between ossicles and maintain their original spatial
152 arrangement. All samples were then rinsed three times in MilliQ water, dehydrated in graded
153 ethanol series and dried. All samples were coated in platinum and photographed using a
154 Philips XL-20 scanning electron microscope (SEM) at the Institute of Paleobiology of the
155 Polish Academy of Sciences in Warsaw, Poland (accelerating voltage ca. = 25 kV, working
156 distance ca. = 34 mm).

157 **2.3. Manganese labeling**

158 Manganese (Mn)-labeling was conducted following the described procedure [11]. Ten
159 individuals (five controls and five experimental) were placed in independent, aerated 1.5 L
160 aquaria (see Fig. S1). The parameters of the seawater (temperature, salinity and
161 electromagnetic force [emf]) were measured three times per day using a WTW Multi 340i
162 multimeter and a Metrohm pH-meter (826 pH mobile) equipped with a combined glass
163 electrode (Metrohm Primatrode), and calibrated everyday with CertiPUR® buffer solutions
164 pH 4.00 and 7.00 (Merck, Darmstadt, Germany). All emf measurements were subsequently
165 converted to pH values following DelValls and Dickson's method [26] with TRIS/AMP
166 buffers. Differences between measured water parameters in the different aquaria were
167 assessed using repeated measures ANOVA. Overall, sea water parameters remained
168 comparable between the Mn-exposed and control groups, with significant changes detected
169 only over time, but not attributable to treatment (see Table S2).
170 Each day seawater was fully replaced in each aquarium. Specimens were fed every second
171 day with soft tissues of mussels. The experiment spanned up to ten days and involved a total
172 of ten specimens (five controls and five experimental). Of these, six specimens (three
173 experimental and three controls) were subjected to the following sequence: one day in normal

seawater, two days of incubation (Mn-enriched seawater for experimental individuals, normal seawater for controls), and a final day of recovery in normal seawater. Two additional individuals (one experimental and one control) underwent an extended post-tagging recovery of three days instead of one. The last two individuals (one experimental and one control) followed the same scheme, with only the experimental individual exposed to a secondary Mn-labeling incubation on days 7 and 8, while the control remained in normal seawater, followed by a 2-day recovery. During labeling, seawater was enriched with manganese using $MnCl_2 \cdot 4H_2O$ (Sigma-Aldrich), dissolved to result in a nominal Mn^{2+} concentration of 3 mg/L. After the experiments, all animals were fixed, rinsed in seawater and then in ultra-pure water before being air dried for 48 hrs at 50°C. Afterwards, they were dehydrated in graded ethanol series (70%, 90% and 100%, each step lasted 2 hrs), and dried again for 48 hrs at 50°C.

2.4. Cathodoluminescence imaging

Thin sections were prepared from two arms randomly selected from each individual, including both experimental and control specimens. Samples were embedded in epoxy resin, and thin sections were prepared using a series of diamond suspensions and finally carbon-coated. They were analyzed with the aid of Lumic HC5–LM cathodoluminescence (CL) microscope equipped with a hot cathode at the Institute of Paleobiology, Polish Academy of Sciences, Warsaw. Images were recorded using a Kappa video camera. An electron energy of 14 keV was applied and, depending on the sample, beam currents between 0.8 – 0.14 mA were used. Exposure times varied between 1.5 and 10 seconds.

Variably oriented D-TPMS lattices within each plate, with stereom trabeculae cut both parallel to their long axis and at oblique angles, were analysed. Sections oriented approximately along crystallographic {111}, {110} and {211} planes of the D-TPMS were found to be the most informative and were therefore used to assess the growth patterns described below.

199 **2.5. Calcium, F-actin, nuclei and α-tubulin labeling**

200 A group of six specimens, not previously used in any experiments, were used for labeling of
201 calcium, F-actin, nuclei and α-tubulin. We followed a slightly modified protocol recently
202 published by Vyas al. 2024 [19]. First, for calcium labeling, animals were incubated alive for
203 24 hours in aerated, independent 1.5 L aquaria, filled with seawater containing calcium-
204 binding fluorescent markers. Two different markers were tested, at a final concentration of
205 300 mg/L: Calcein Blue (Sigma Aldrich - M1255) and Xylenol orange (Sigma Aldrich -
206 1086770005), both of which bind to newly deposited calcium. This concentration is
207 comparable to that used by Vyas et al. (2024) [19], who applied 250 mg/L. To mitigate the
208 impact of Calcein Blue on seawater pH, sodium bicarbonate solution was added to maintain
209 pH at ca. 8.0. Both markers proved effective in all specimens and provided similar results (see
210 Results section). Following incubation, for F-actin, nuclei and α-tubulin labeling, all animals
211 were rinsed for 30 minutes in aquaria containing fresh seawater. No mortality was observed.
212 For each specimen, two arm tips and two spines (knob-shaped arm tubercles of carinal plates)
213 were collected using a sharp blade. Samples were fixed in 4% paraformaldehyde (PFA)
214 solution for 30 minutes at room temperature (RT). The solution was prepared diluting in
215 MFSW a stock solution of PFA 8% prepared in MilliQ distilled water. Next, all samples were
216 rinsed five times for 5 minutes each at RT using the following proportion of Millipore filtered
217 seawater (MFSW) to Phosphate-Buffered Saline (PBS): 1:0, 3:1, 1:1, 1:3 and 0:1. Samples
218 were then rinsed four times for 5 minutes each at RT in 1x PBST (PBS 1x, 0.05% Tween20),
219 before being pre-blocked for 1 hour at RT in 1x Bovine Serum Albumin (BSA) solution in
220 PBS. For F-actin staining we used Phalloidin (1:100) coupled with four different dyes: iFluor
221 405, ALEXA Fluor 647, ALEXA Fluor 555plus and ALEXA Fluor 633 (Thermo Fisher
222 Scientific). For nuclei labeling, samples were incubated in 4',6-diamidino-2-phenylindole
223 (DAPI) (Thermo Fisher Scientific) (1:500). For α tubulin labeling, we used anti-α-tubulin

antibodies already coupled with FITC (1:100), as referenced by Vyas et al. (2024) [19]. For those labeling, upon blocking, samples were incubated overnight at 4°C. All stainings were carried out separately or concomitantly depending on the need. Following labeling, samples were rinsed three times 5 minutes each at RT. Confocal micrographs were obtained using a ZEISS LSM 780 and different magnification water objectives ranging from 20X to 63X, at the Matière et Systèmes Complexes Laboratory UMR 7057 in Paris. Fluorescent labeling was excited using 405, 488, 543 or 633 nm lasers usually acting on two or three different and independent scanning sequences. Z-stack was acquired with an interval of 0.57 µm and was later examined using ImageJ Software [27].

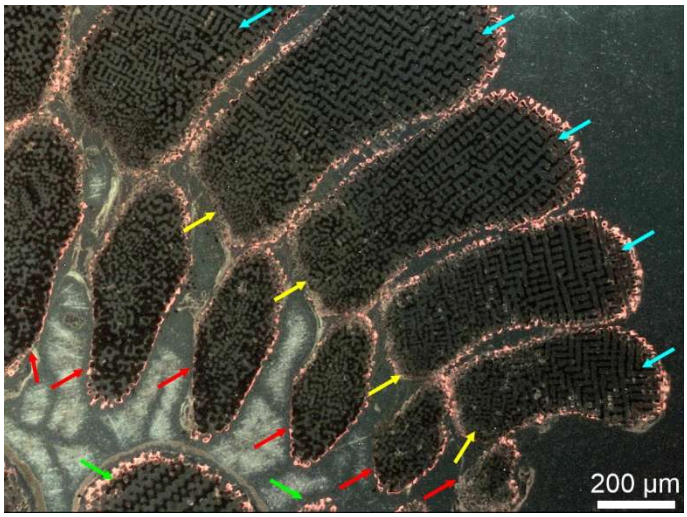

Fig.1. Example of a cathodoluminescence image of a thin section cut along the longitudinal axis of the distal arm portion. Mn-induced luminescent skeleton appears as a bright orange signal; black and dark grey regions indicate skeleton grown in normal (without Mn^{2+}) seawater and resin with soft tissues, respectively. Arrows indicate the following features: green – partially visible carinal plate composed of diamond-type stereom, red – ambulacral plates composed of labyrinthic (unordered) stereom exhibiting regional differences in porosity density, yellow – labyrinthic stereom in the internal portion of the

distal adambulacral plates, blue – diamond-type stereom of the adambulacral plates. [single column image]

3. Results

3.1. Microstructural observations by Scanning Electron Microscopy (SEM)

The skeletal organization of *Protoreaster nodosus* comprises several distinct types of plates (see Fig. S3). As previously reported [20], we observed that the carinal, inferomarginal, superomarginal, dorsolateral, and adambulacral plates exhibit the same diamond-type (D-TPMS) stereom, whereas the ambulacral plates display labyrinthic stereom (Fig. 1, Fig. S3). All of these plates are further covered by small covering spinelet plates bearing less organized galleried stereom (Fig. S3).

Following [20], the porous lattice of plates with D-TPMS geometry can be described as a network of nodes (points where a variable number of trabeculae converge) and branches (trabeculae connecting two nodes), for which both width and length can be quantified. In the D-TPMS lattice analyzed here, the predominant node type is N4 - a node connected to four branches (Figs. 2-4). These nodes are arranged in tetrahedral coordination along the {111} crystallographic direction: the basal vertices of the tetrahedron and the apical vertices extending along {111} (as seen on Fig. 3A, B; Fig. 4).

SEM imaging allowed us to study the spatial distribution of skeletal structures and stereom microarchitectures preserved at different developmental stages (Figs. 2-5). Through high-resolution SEM imaging of plate surfaces, we observed repetitive stereom structures associated with distinct patterns of stereom growth, consistently appearing on all D-TPMS-bearing plates. However, elucidating the formation mechanisms of these structures required integrating data from both SEM and cathodoluminescence studies (see subchapter 3.3).

On every plate exhibiting D-TPMS stereom lattice, three main patterns of diamond-type stereom growth were observed (see Fig. 2): (1) here termed trifurcation, which is a stereom growth resulting in the formation of successive layers roughly elliptical in shape) and occurring on flat external surfaces of plates oriented approximately along the {111} planes of the D-TPMS (Fig. 2, Fig. 3A). (2) here termed bifurcation, which is a growth pattern that appears to be supplementary to trifurcation, typically occurring around the edges of external surfaces of plates or between trifurcating regions on surfaces of varying shape, roughly aligned with the {100} planes of the D-TPMS lattice (Fig. 2; Fig. 3E); (3) an intermediate growth pattern, which is present at the borders between tri- and bifurcating regions, and exhibits a combination of characteristics from both growth types (Fig. 2A, & B). It is worth noting that if the D-TPMS microarchitecture ultimately results from marginal (surface-driven) growth, the range of viable geometric configurations becomes inherently limited, which is consistent with the emergence of bifurcating and trifurcating growth patterns along defined orientations.

Layers in trifurcating regions consist of nodes extending laterally and apically. Each node in lateral vertices (hereafter referred to as crown node) connects to three nodes in apical vertices (hereafter referred to as budding nodes) of the same layer and one budding node in the layer below, while each budding node connects to three crown nodes in the same layer and one crown node in the layer above (Fig. 4). During growth, crown nodes form on top of the branch extending from a budding node, and branches extending from the crown node connect with each other, forming new budding nodes while maintaining the tetrahedral connectivity. This process will be explained in detail in chapter 3.3.

All aforementioned plate types exhibiting D-TPMS were found to further contain small volumes of irregular, unordered labyrinthic stereom (see Fig. S4). These regions are typically located within the interior and exhibit ellipsoidal shapes. They are clearly distinct in both size

and trabecular thickness from the D-TPMS stereom (which usually displays some minor dislocations [20]). In adambulacral plates, the labyrinthic stereom is located in the internal portion of the plate. The morphogenesis of the labyrinthic stereom has not been explored here.

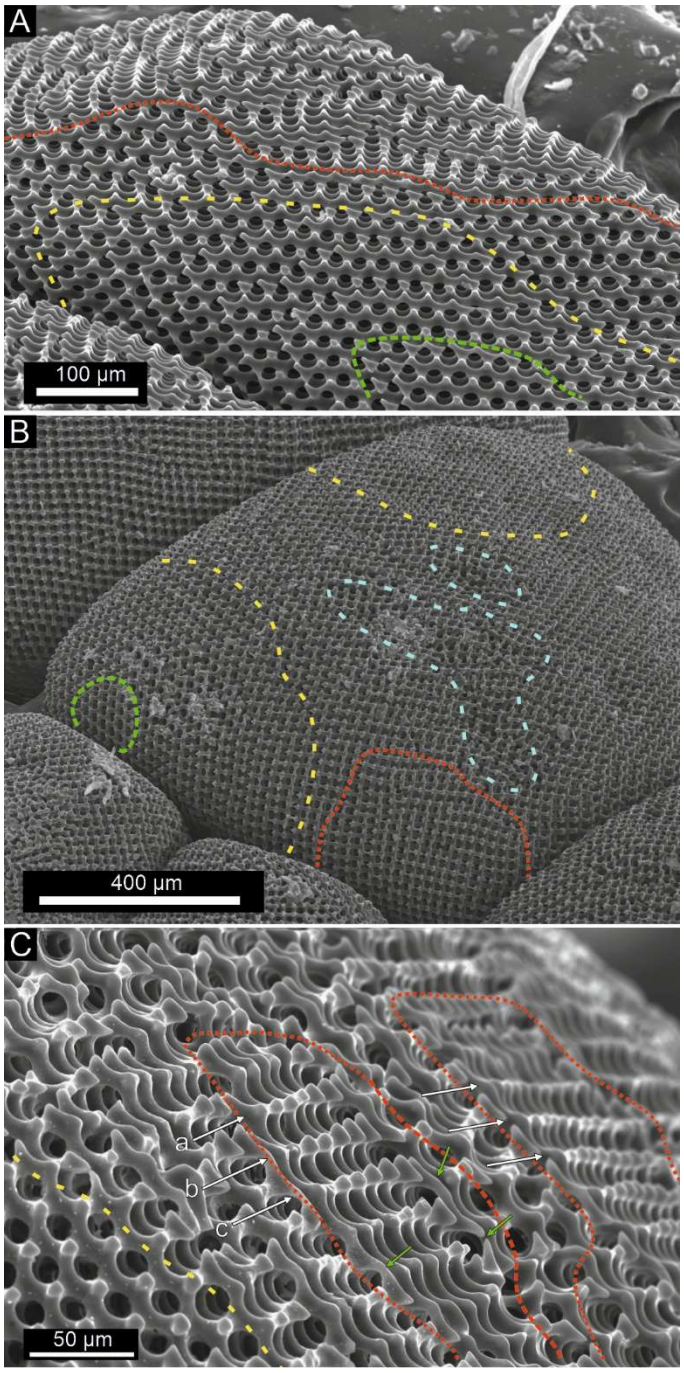

Fig. 2. SEM images of superomarginal plates, orientated nearly along the {110} (A) and {100} (B) planes of D-TPMS, and with enlargement of different growth regions on the outer surface of trabeculae (C). Dashed lines highlight distinct growth regions: green – a trifurcating layer, yellow – approximate extent of trifurcating region; red – approximate extent of bifurcating regions, cyan – a rare occurrence of irregular stereom visible on the surface. The area between red, yellow and cyan boundaries exhibits intermediate growth patterns. White arrows in (C) indicate exemplary bifurcating rows, some of which were denoted (a-c); in each of those a steady progression of growth is observed from a node in the lower left (indicated by arrow) to the node in the upper right. Green arrows mark newly formed trabecular arches (see Discussion). [single column figure]

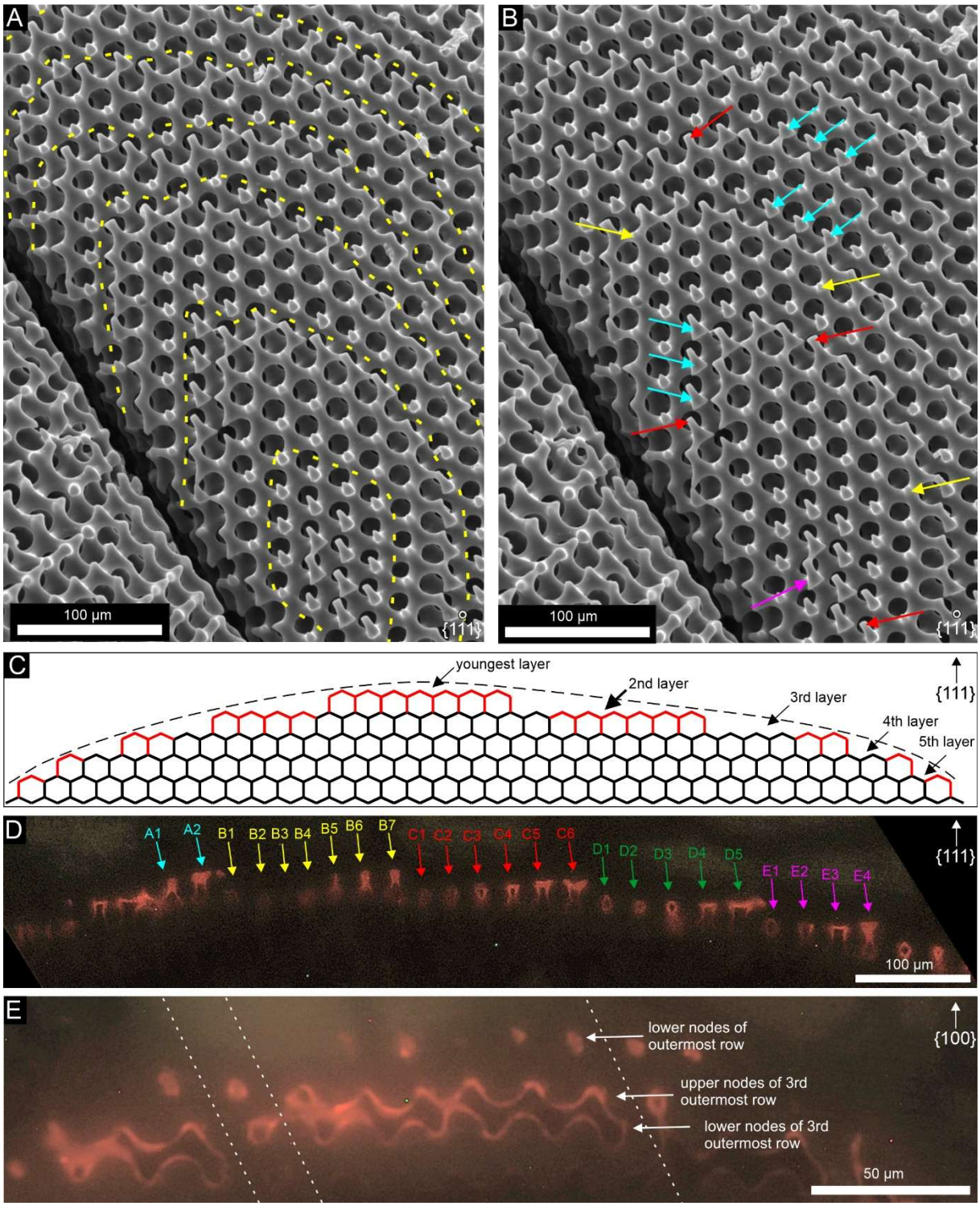

Fig. 3. Trifurcating (A-D) and bifurcating (E) regions of the D-TPMS. (A, B) Same region of superomarginal plates viewed along their {111} plane. In (A), yellow dashed lines demarcate the approximate boundaries of successive layers and, in (B), arrows point to the group of nodes forming a new uppermost layer (magenta), to proto-nodes (red), "dormant

nodes" (yellow) and crown nodes (cyan) growing at the edges of expanding layers (for definitions see subchapter 3.3). (C) Simplified scheme of trifurcating growth dynamics, based on compilation of data from CL studies. Stereom lattice is depicted as viewed in a thin section perpendicular to the {111} plane of D-TPMS. Growing trabeculae and thickening growth have been omitted. Black branches represent all trabeculae formed prior to the biomineralization of the red-colored trabeculae. The red branches correspond to trabeculae that formed within a short time interval (2-3 days). The thin dashed black line outlines the margin of the growing plate. (D) Surface of an inferomarginal plate, exhibiting an active trifurcating region: thin sections cut roughly perpendicularly to the {111} plane of D-TPMS. Arrows labeled with numbers mark the oldest (e.g., A1, B1) and youngest (e.g., A2, B7) trabeculae located at the respective edges of each highlighted layer. (E) Surface of a different inferomarginal plate, within an active bifurcating region. White lines separate angular unconformities on the thin section. [double column figure]

3.2. Cathodoluminescence analysis of stereom growth patterns

Manganese (Mn) labeling followed by cathodoluminescence (CL) imaging has previously been shown to be an efficient method for tracking stereom growth dynamics at the microstructural scale in echinoderms [11]. In adult starfish, Mn-stained stereom was consistently well-differentiated under CL, in all thin sections taken from the arm fragments of specimens in the main experimental group (Fig. 1), with staining being detected in every marked specimen. In contrast, the stereom of the control group showed no Mn-induced luminescence (see Fig. S5).

The skeleton labeled with Mn exhibits distinct, bright orange luminescent increments at the plate periphery, indicating that skeletal growth and Mn incorporation occurred during the two-day incubation treatments. In contrast skeletal growth during the one-day recovery period, in

342 the main experimental group, was rarely observed in the examined plates, indicating a delay
343 in biomineralization upon Mn^{2+} exposure, likely caused by the equilibration of manganese
344 pools between ambient seawater and internal tissues of starfish. Note that a single individual
345 incubated for an extended (3-day) recovery period exhibited somewhat more pronounced and
346 clearly detectable non-luminescent skeletal growth following the tagging event (see Fig. S6).
347 In contrast, another specimen subjected to two separate Mn-labeling events yielded
348 inconclusive results regarding non-luminescent skeletal growth, as no clearly distinguishable
349 two growth increments were consistently observable.
350 Precise quantification of growth rates was hindered by orientation-dependent variability of the
351 sectioned surfaces, which introduced measurement bias. Nevertheless, the rate of progression
352 of both tri- and bifurcating growth fronts appeared to vary with plate type and anatomical
353 position within the arm, ranging from several to tens of micrometers per day, and were highly
354 dependent on factors such as the individual specimen, plate size (or inferred age), and specific
355 location on the plate. Only on some surfaces a continuous, evenly thick stereom
356 (approximately twenty micrometers thick) was formed during labeling (see Fig.1 blue arrows)
357 while on other plates the Mn-induced luminescent growth fronts contained gaps (see Fig. 3D).
358 Thickening of previously formed stereom trabeculae (including both longitudinal trabeculae
359 and lateral bridges) was also well visible, and could extend up to several tens of micrometres
360 below the areas where trabecular tips were forming. In general, the peripheral growth was
361 most pronounced in the distal plates.
362 Despite these uncertainties, we were able to identify a general growth pattern and formulate
363 hypotheses concerning its dynamics. For instance, if we define the growth rate as the change
364 in the trifurcating layer radius over the measured time interval, one observes that the growth
365 rate decreases with each subsequent layer (see Fig. 3C, D), relative to the ring thickness, in
366 order to maintain the surface curvature. Considering the minimal size differences between

367 layers, the minimal observed growth rate was ca. ~15 µm/2 days (corresponding to the
368 incorporation of a single new crown node within that time frame). The maximal observed
369 growth rate of a pre-existing (second youngest) layer in one direction was approximately 100
370 µm/2 days, equivalent to 3-4 newly incorporated crown nodes. Conversely, defining the
371 growth rate globally, as the number of new nodes (red in Fig. 3C & D) along a line
372 perpendicular to the dashed envelope, showed that it remains approximately constant (one
373 node per period) within the resolution of our measurements, explaining the preservation of the
374 overall dome shape.
375

376 **3.3. Stereom growth patterns**

377 As mentioned before, the information obtained through SEM was complementary to CL
378 imaging, with SEM providing high-resolution details of stereom architecture, while CL
379 allowed the determination of the sequence of stereom formation (see also Fig. S7). The
380 following subsections present these observations in detail, integrating data from both
381 techniques - collected from five individuals subjected to Mn labeling and two individuals
382 examined using SEM.
383

384 **3.3.1. Trifurcating stereom growth**

385 Trifurcating growth was only observed on external surfaces of plates oriented along the D-
386 TPMS planes belonging to the crystallographic {111} family. Most prominently, it occurred
387 when the surface of the plate was oriented at an angle between 0° and 30° to the {111} plane,
388 around which it became less distinguishable and was progressively replaced by bifurcating
389 growth mode, which became most pronounced at the plate surface inclined at an angle 30° to
390 45° relative to the {111} plane. When viewed from the top (Fig 3A), along the {111} plane of
391 the D-TPMS, the stereom formed by this mode of growth appeared as a bundle of layers

stacked upon one another (Fig. S7). The outermost layer in this view, corresponding to the trifurcating region, represented the youngest stage of growth.

As pointed out above, each fully developed crown node is connected to three budding nodes within the same layer and one budding node from the layer below. Conversely, each fully developed budding node is connected to three crown nodes within the same layer and one crown node from the layer above (Fig. 4 Stage 1). When such a layer reached a certain width, few budding nodes located near its center (presumably the oldest from the previous generation) - simultaneously formed small protrusions (buds) that elongated vertically along the crystallographic {111} direction, which corresponds to the *c axis* of the constituent calcite at the atomic scale, giving rise to vertical branches directed upwards (Figs. 3B, S7 and Fig. 4 Stage 2). At the tip of each branch, a new crown node formed (Fig. 4 Stage 3). These new crown nodes then trifurcated (Fig. 4 Stage 4), creating three small lateral protrusions. From each new crown node, one of these protrusions was growing visibly faster (Fig. 4 Stage 5) and eventually formed at their tip a node-like structure, hereafter referred to as a proto-node. New proto-nodes in a given trifurcating region consistently emerged along the same direction (Fig. 3B; Fig. S7). Depending on their location, proto-nodes can thus grow toward (e.g. Fig. 3: lowermost red arrow; Fig. S7, blue nodes in the middle), outward (Fig. 3: uppermost red arrow) or along the layer margin (Fig. 3: two other red arrows), with the latter case being most common on all plates due to the D-TPMS stereom geometry. Subsequently, if another branch or branches from a nearby crown nodes are available for coupling, they connected to the proto-node that ultimately became a new budding node (Fig. 4 Stage 6).

After forming its core, each layer expanded peripherally by incorporating additional crown nodes that budded from the underlying layer in a circular pattern around the growing layer (Fig. 3B). Thus, zones of active trifurcating growth formed concentric rings around the periphery of each layer, spreading outward horizontally like ripples, as the layer increased in

size. The horizontal growth of each layer remained approximately isotropic until it approached the plate edge where a non-trifurcating region begins (see Fig. 2A). Budding nodes located between active growth zones remained “dormant”, exhibiting only thickening growth of trabeculae until they reached their maximum width. In general, each successive pair of layers exhibited a decreasing size difference, leading to progressively thinner “rings” of exposed nodes in each subsequent layer (see Fig. 3A, C). The minimal ring width (~30 µm) was observed when it consisted of a single line of exposed budding nodes. This is consistent with marginal growth, occurring mainly at the edges of the 3D structure of the ossicle, i.e., normally to the dashed envelope sketched in Fig. 3C.

The active, thickening, and dormant zones can be observed on CL images (Fig. 3D, E). In these images, the manganese signal was most prominent on the edges of each layer, where nodes and branches were composed entirely of manganese-induced luminescent calcite (active zones) (e.g. Fig 3D, nodes B6-B7 and C5-C6). Few preceding nodes in each layer might also exhibit distinct luminescence, but only on their outer surfaces, which indicates that these nodes underwent only thickening growth during the staining period (thickening zones) (e.g. Fig. 3D, nodes C3-C4). The remaining exposed budding nodes of each layer showed dull or no luminescence, suggesting that no growth occurred during that time (dormant zones) (e.g. Fig. 3D, nodes B1-B4 and C1-C2). The number of those nodes in a layer and the time they spent in “dormant” phase varied depending on the shape of the plate and the size of the layer, however, this duration, based on CL images, can be approximated to range from a day to a week.

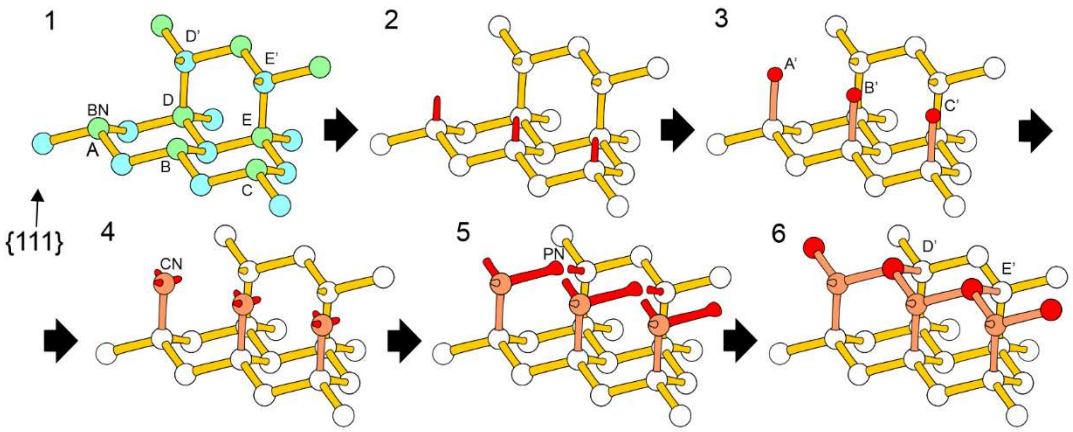

Fig. 4. Simplified 3D diagram illustrating successive stages of trifurcating growth localized at the edge of a pre-existing layer, in a plate exhibiting D-TPMS. Nodes are represented with small spheres and branches with cylindrical rods, thus their thickness and length do not represent their actual proportions. Color code: light blue – crown nodes; light green – budding nodes (color distinction shown only in the first panel); yellow – pre-existing branches, that are no longer elongating; white – pre-existing, fully formed nodes; red – nodes and branches undergoing elongation/thickening; orange – nodes and branches that were formed within the depicted time frame, but are no longer elongating. In the figure, we depicted budding nodes from the lower layer (A, B, C, D, E) and crown nodes that grew out of them, belonging to the upper layer (A', B', C', D', E'), as well as all branches and nodes connected to those ten nodes at the given stage. In the first picture, nodes A, B, C are illustrated at stage 1, nodes D and E are fully developed and nodes D' and E' are at stage 6. Other, undefined nodes are fully developed. The symbols BN, CN, and PN were used to denote representative budding node, crown node, and proto-node, respectively. Stage 1. Each budding node (A, B, C) connects only to three crown nodes within the same layer. Stage 2. A budding protrusion emerges upwards along the *c axis* of calcite from the top of the budding node. Stage 3. A crown node is formed at the tip of the budding protrusion, being noticeably thicker than the budding branch. The original budding node, now connected to four nodes, will no longer develop except for thickening. All further stages refer to the set of newly

formed crown nodes (A’, B’, C’). Stage 4. Three protrusions can be distinguished at the top of the crown nodes (around this time, the next set of budding nodes, which are not shown in the diagram, would begin advancing from stage 1 to stage 2). Stage 5. The trifurcating branches elongate and one becomes distinctly longer and thicker at its tip, forming a proto-node (proto-nodes in this diagram are orientated along the layer edge). Stage 6. Branches extending from the crown nodes connect with other adjacent branches, and the developing crown nodes are incorporated into the upper layer. After these connections, nodes D’ and E’ finish their development and only thickening is observed on existing branches. Similarly, nodes A’, B’ and C’ finish their development only after the next set of crown nodes reaches stage 6. Stages 1-3 describe three lower-layer nodes (A, B, C), while stages 3-6 correspond to crown nodes (A’, B’, C’). Proto-nodes, which have connected to two adjacent branches emerging from the nearby crown nodes, form new budding nodes in the upper layer. The minimal estimated (based on CL images) time for progression from a budding node at the beginning of stage 2 to a crown node at the end of stage 6 is approximately 12 hours. [two column figure]

3.3.2. Bifurcating stereom growth

As previously mentioned, bifurcating growth is considered supplementary growth, occurring on surfaces orientated at ca. 30-45° angle to any of the {111} planes, where uniform trifurcation is not supported. In contrast to trifurcating regions, which possess a fixed central point, concentric growth zones surrounding it and distinct layers, bifurcating regions exhibited a seemingly irregular growth that only locally exhibited repeating structures (Fig. 2C). As such, bifurcating growth regions could have only been seen as a patchwork of linear rows of different length, which grew by extending one or both of their ends.

The bifurcating growth pattern was most clearly observed in two adjacent, parallel rows as sketched in Fig. 5. Growth initiated from the oldest budding nodes in each row (Fig. 5 Stage

1), giving rise to small protrusions (Fig. 5 Stage 2), which subsequently extended into branches (Fig. 5 Stage 3). As the two branches elongated, they further gradually inclined toward each other (Fig. 5 Stage 3) and as a result connected to each other (Fig. 5 Stage 4). Upon connecting, an initial arch-like structure lacking a distinct central node was formed (Figs. 2C (green arrows); and Fig. 5 Stage 4). Ultimately, a new node formed upward from the apex of this arch (Fig. 5 Stage 5).

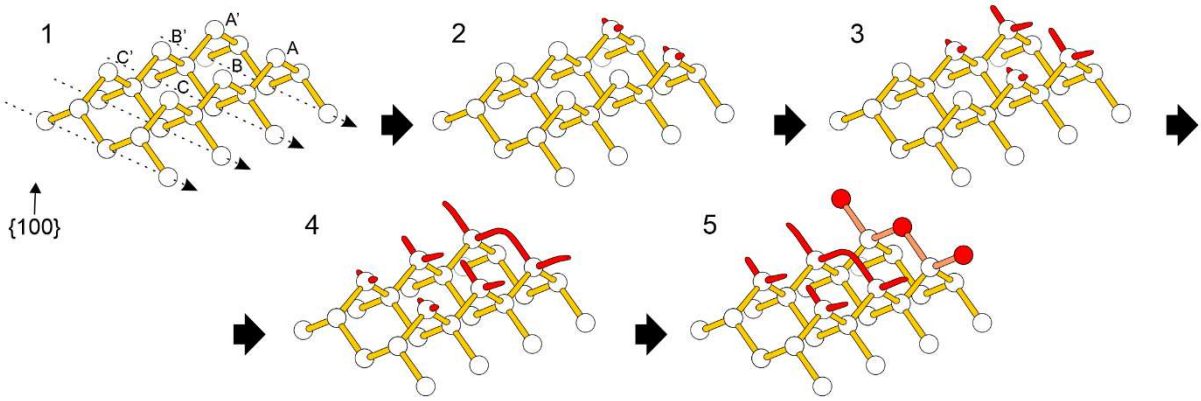

Fig. 5. Simplified 3D diagram showing sequential stages of bifurcating growth across three node generations in a plate exhibiting D-TPMS. Node and branch thicknesses and lengths are not representative, as explained in Fig. 4; colors follow those of Fig. 4. Stage 1. The upper nodes in two parallel rows (A-C, A'-C') are connected to two bottom nodes in the same row. Here, six rows are illustrated: four lower (marked by arrows), and two higher, perpendicular to them (containing nodes A–C and A'–C'). Stage 2. Two side branches emerge from two oldest upper nodes (A, A'), forming a straight top ridge perpendicular to the row. Stage 3. Branches extend and, while growing, incline slightly toward adjacent nodes, while at the same time the subsequent upper nodes start stage 1. Stage 4. At least one branch connects with that of a neighboring node, forming an arch-shaped skeletal bridge. Stage 5. A new node

develops from the top of the arch. The new node enters stage 1, starting the next cycle. Nodes B, B', C, C' and subsequent pairs (not shown on the diagram) continue to grow until, one after another, they reach stage 5. In this way, growth waves propagate along each row, generating surfaces of parallel node series. Growth typically proceeds at a steady pace during stages 1–2, then accelerates within stage 2. Longer bifurcating series show most nodes at stages 1 or 2 (see Fig. 2C - therein rows a-c contain 2-3 such nodes each, then row c includes a stage 4 node; rows a and b reach stage 5) [Two-column figure]

3.4. Confocal observations - overall characterization

To gain insights into the potential involvement of the cytoskeleton in stereom growth, regardless of stereom type, and in particular at the level of individual trabeculae and their fusion processes, we next performed a series of staining targeting F-actin filaments and microtubules. Along these staining, we further labeled nuclei and newly biomineral deposition of calcium, to concomitantly visualize trabecular growth. We found, as previously reported [9, 19], the accumulation of calcium located at the growing tips of trabeculae (Fig. 6 & Fig. 7). Furthermore, we observed that cell nuclei were commonly localized near the base of the growing trabeculae (Fig. 6), rather than at the growing tips, and showed a loosely dispersed pattern therein with no evident spatial regularity. Microtubules, in turn, appeared arranged in bundles, predominantly oriented longitudinally along the trabeculae (Fig. 6A). However, although the α-tubulin signal was typically strong at the onset of image acquisition, it exhibited thereafter rapid deterioration upon increased laser power and depth imaging, impairing further analyses. By contrast, cytoskeletal labeling carried out for F-actin, revealed a similar spatial distribution and three-dimensional organization of F-actin filaments on the growing surfaces of both the diamond-type stereom-bearing plates (carinal, inferomarginal, superomarginal and dorsolateral and adambulacral) and the less-ordered galleried stereom-

529 bearing covering spinelet plates (Fig. 6, Fig. 7). A consistent pattern emerged across all
530 observed plates and stereom types in all six marked specimens: F-actin densification was
531 localized at the tips of actively growing trabeculae (identified by strong calcium-related
532 fluorescence signal) regardless of plate morphology or underlying stereom microarchitecture.
533 In the galleried stereom of spinelet plates, the intensified F-actin signal appeared as minute
534 caps positioned a few micrometres above the tips of growing trabeculae, or as catenoid-
535 shaped structures forming between adjacent elongating branches (Fig. 6). In diamond-type
536 stereom, F-actin signals were also detected at the tips and in between trabeculae, where they
537 form several recurring structural morphotypes (ranging from thin, disordered bundles to
538 catenoid-like tubular structures, and sheath-like coatings), which seem to be related to specific
539 developmental stages of the associated trabecular tips (Fig. 7).
540

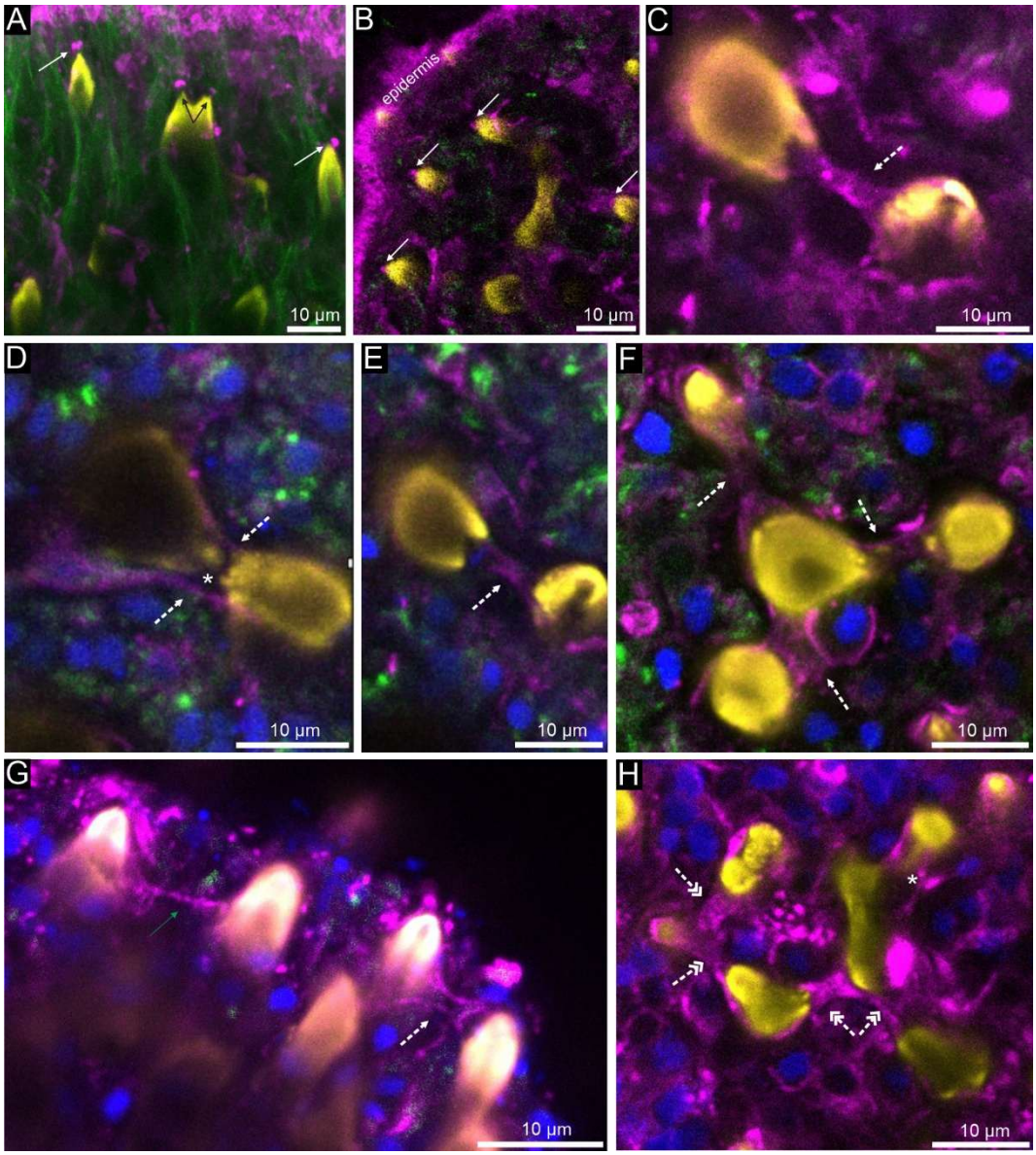

Fig. 6. Confocal images of galleried stereom in spinelet plates of an adult starfish showing F-actin densification in growing trabecular tips and between trabeculae. (A, B) Zoom-ins of F-actin caps located at the tip of growing trabeculae. (C-H) Zoom-ins of F-actin catenoid-shaped filaments connecting adjacent growing trabeculae or wrapping adjacent trabecular bridges. Yellow – freshly biomineralized skeleton, blue – nuclei, magenta – F-actin, green – α-tubulin, white plain arrows – F-actin caps, black arrows – trabecular tips, dotted white arrows – F-actin catenoid bridges, * – sheath-like coating of trabeculae, dotted white double arrows – complex F-actin catenoid bridges, green arrow – thin F-actin filament. [1.5 column figure]

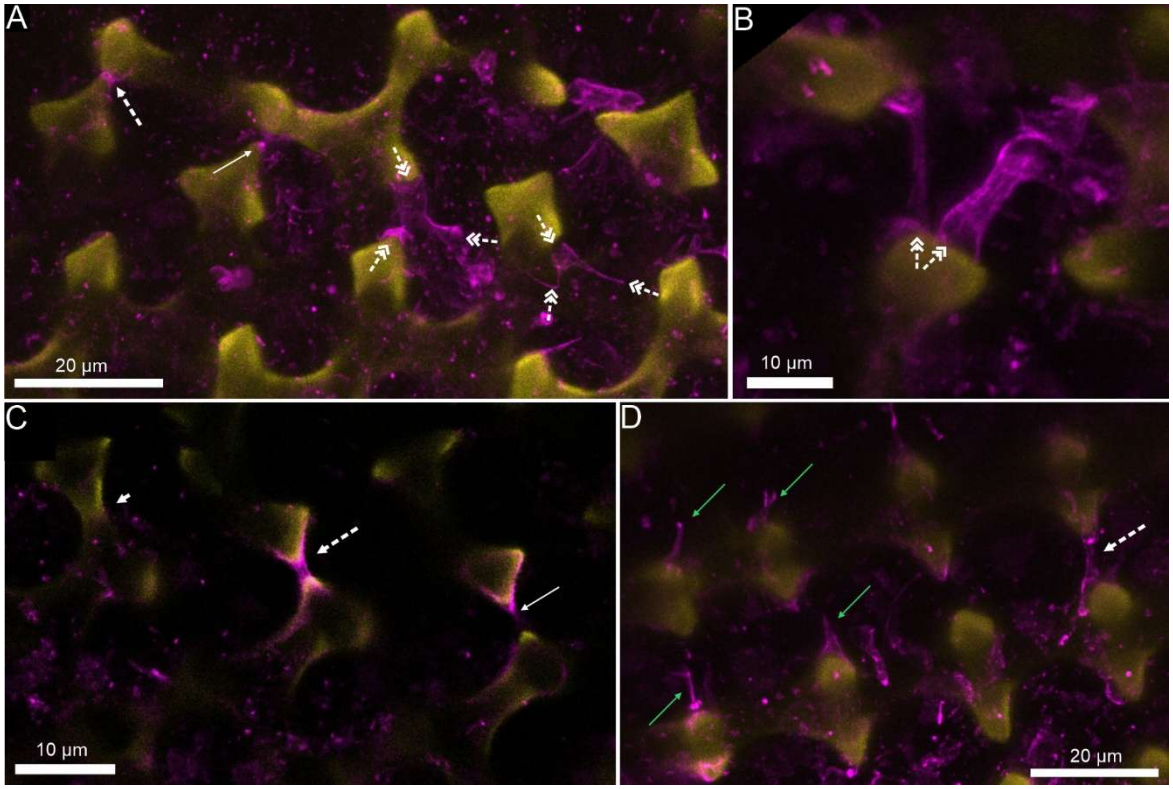

Fig. 7. Confocal images of F-actin densification in growing trabecular tips in active growth zones of diamond-type stereom in adambulacral plates of an adult starfish. (A, B) Trifurcating zones. (C, D) Bifurcating zones. Arrows highlight a variety of F-actin structures possibly at different stages of development. Yellow – freshly biomineralized skeleton, magenta – F-actin, white plain arrows – F-actin caps, dotted white arrows – F-actin catenoid bridges, white plain short arrow – fully developed trabecular calcite bridge without F-actin coating, dotted white double arrows – complex F-actin catenoid bridges, green arrow – thin F-actin filament. [2 columns figure]

4. Discussion

As noted by Yang et al. (2022) [20], the formation mechanisms of diamond-type stereom have not been systematically explored, and understanding these processes would be of great value not only to the materials science community, but also to a broader audience across

566 multiple scientific domains. Here, we provide the first detailed characterization of these
567 morphogenetic processes, demonstrating that ossicle formation bearing diamond-type stereom
568 can be described in terms of two fundamental growth modes: trifurcation and bifurcation.
569 While progressing on different distinct planes, these growth modes are synchronized,
570 ultimately generating a coherent D-TPMS lattice. Trifurcating growth can be divided into six
571 identifiable stages, as visualized in Fig. 4; it should be noted that the sequence is qualitative
572 and does not imply a constant growth rate or a uniformly distributed timeline. Similarly,
573 bifurcating growth can be described in terms of five observable stages, depicted in Fig. 5,
574 with the same caveat regarding the qualitative nature of the sequence.
575 Building upon the delineated growth patterns of ossicles, we further explored the cytoskeletal
576 dynamics that is linked to trabecular formation. We found that intensified F-actin signals at
577 the tips of growing trabeculae were consistently observed at active growth fronts in both
578 diamond-type and less-ordered galleried stereom of *Protoreaster nodosus* (Fig. 6 & Fig. 7).
579 These findings corroborate some earlier reports documenting F-actin accumulation at
580 biomineralization sites in echinoid embryos and holothuroid juveniles [16-19], while
581 representing the first visualization of F-actin distribution in asteroid skeletal elements. The
582 possibility that F-actin participates in initiating or guiding trabecular growth and connections
583 within echinoderm stereom has only recently been proposed [19] and still requires more
584 thorough documentation. Thus, the observations presented here not only support the
585 hypothesis of a key role for the cytoskeleton in echinoderm biomineralization [17-19], but
586 also suggest actin-mediated structural templating/guiding in the form of caps and catenoid-
587 like bridges during stereom morphogenesis.
588 In general, F-actin structures associated with elongating trabeculae can be classified into two
589 categories: (i) caps, which are situated immediately above or closely associated with growing
590 trabecular tips, and (ii) bridges, which connect two opposing growing trabeculae. Both

591 categories exhibit some variability in shape and size, likely reflecting differences in
592 developmental stage and growth dynamics.
593 F-actin accumulation was consistently observed across all skeletal plates, irrespective of
594 whether they contained galleried stereom (e.g., spinelet covering plates) or diamond-type
595 stereom , the morphogenesis of which was explored in detail herein. In both stereom types, F-
596 actin caps appear as loosely hemispherical or open conical concentrations, typically thinner
597 than the underlying trabecular protrusions and positioned up to about a few micrometres
598 above the trabecular tips (Fig. 6 & Fig. 7). Notably, thread-like projections composed of
599 membrane and F-actin forming between the tips of growing trabeculae have recently been
600 documented in juvenile holothurians [19]. Those projections were notably occurring only
601 between approaching trabeculae, suggested to enable their curved growth and eventual fusion
602 [19]. In our study, we demonstrate that within these projections, which were also
603 distinguished only between approaching trabeculae, F-actin forms however structurally
604 distinct cytoskeleton bridges, which likely guide and template the ongoing biomineralization
605 of the stereom lattice. We observed F-actin in various forms, thus potentially in different
606 organizational stages, ranging from thin, disordered bundles (Fig. 6G) to catenoid-like tubular
607 structures (Fig. 6C & H and Fig. 7C), and, hypothetically, even to a sheath-like coating (Fig.
608 6D & E) filled with newly deposited mineral. Furthermore, we observed complex catenoid-
609 like bridges between multiple neighboring trabeculae (e.g., Fig. 6H). In trifurcating regions of
610 D-TPMS, specifically between proto-nodes extending from the crown node (outward to the
611 layer margin) and two nearby budding nodes, these bridges exhibit a “pants-like” morphology
612 (Fig. 7A & B). Together, these observations provide new insights into the dynamic processes
613 underlying the formation of these structures. However, a detailed understanding of the
614 developmental progression of these structures will require further investigations. In the
615 Supplementary Materials (Fig. S8 & S9), we present hypothetical, simplified representations

of the F-actin structures observed during trifurcating and bifurcating growth, organized according to their putative developmental stages. These models, however, require additional experimental validation in future studies.

Interestingly, the most commonly observed structure was the F-actin catenoid-like bridge (e.g., Fig. 6C-H; Fig. 7C), herein referred to as a "catenoid bridge". In *Protoreaster nodosus*, catenoid bridges were observed in both galleried and diamond-type stereom, consistently forming between pairs of trabecular protrusions emerging from neighboring nodes prior to trabecular branch fusion at that site. Notably, the catenoid is a classic example of a minimal surface. We hypothesize that the tension exerted by F-actin filaments may impose a characteristic catenoid geometry, which in turn could coherently drive the formation of the stereotypical saddle-shaped morphology of trabecular surfaces. Given that saddle-shaped surfaces are a common feature across all stereom types, we further speculate that this geometric motif may be a consequence of actin-based templating governed by tension-dominated cytoskeletal dynamics. Interestingly, similar actin-mediated processes have been observed in mammalian vascular systems. For instance, Morgulis et al. [27] demonstrated that VEGF (Vascular Endothelial Growth Factor) signaling involved in tubulogenesis may represent a conserved mechanism shared between spicule formation in sea urchin larvae and blood vessel development in mammals, hinting at a deep evolutionary link between biomineralization and vascular morphogenesis. Notably, it has recently been suggested [28], although without experimental verification, that the tension of the soft tissue in sea urchins (stroma) could play a critical role in stereom morphogenesis and its saddle-shaped surfaces.

5. Conclusions

Altogether, our findings reveal that, in the adult starfish *Protoreaster nodosus*, the formation of plates (or ossicles) bearing diamond-type stereom proceeds via two primary growth

641 patterns, which we named trifurcation and bifurcation. These two patterns develop on distinct
642 planes across the plate surface, although they are yet coordinated to form a coherent D-TPMS
643 lattice. Overall, plate growth is highly dynamic, exhibiting localized variation in growth rate,
644 which points to a high degree of cellular control over biomineralization. We demonstrate that
645 such control is highly localized at the growing front and is likely mediated by the
646 cytoskeleton. Indeed, irrespective of plate or stereom type, F-actin densification consistently
647 localizes at sites of active biomineralization, particularly at elongating trabecular tips, thereby
648 strongly supporting previous findings that underscore a critical role of the cytoskeleton in
649 stereom morphogenesis. Furthermore, in certain regions, the formation of F-actin catenoid-
650 like bridges precedes the development of lateral connections between adjacent stereom
651 trabeculae, suggesting a potential role in triggering and templating trabecular fusion. We
652 hypothesize that the cytoskeleton exerts a significant modulatory function in stereom growth,
653 influencing also its characteristic saddle-shaped minimal surface geometry. Specifically, the
654 tension generated by F-actin filaments may impose a distinctive catenoid form (analogously
655 to what has been observed at larger scales in mammal tissues [29]), which in turn directs the
656 stereotypical saddle-shaped morphology of trabecular surfaces. Given that saddle-shaped
657 surfaces are a conserved feature across all observed stereom types, we further speculate that
658 this geometric motif arises from actin-based templating governed by tension-dominated
659 cytoskeletal dynamics. Because of the recurrent involvement of the cytoskeleton in
660 biomineralization across diverse lineages, including silicifying diatoms [30], calcifying algae
661 [31, 32], foraminifers [33], and echinoderms [19, this study], it is likely that F-actin, in
662 particular, plays a fundamental and evolutionarily conserved role in these processes.
663

664 **Declaration of Competing Interest**

The authors declare that they have no known competing financial interests or personal relationships that could have appeared to influence the work reported in this paper.

Acknowledgements

The project was funded by NCN grant 2023/51/B/ST10/01640. Ph.D. is a Research Director of the National Fund for Scientific Research (Belgium). We thank members of the laboratory of Marine Biology at ULB for help in performing experiments.

CRediT authorship contribution statement

Kamil Humański: Conceptualization; Formal analysis; Investigation; Methodology; Visualization; Writing - original draft; and Writing - review & editing. Giulio Facchini: Conceptualization; Formal analysis; Investigation; Methodology; Visualization; Writing - review & editing. Jenifer Croce: Conceptualization; Methodology; Writing - review & editing. Dorota Kołbuk: Formal analysis; Investigation; Methodology; Supervision; Writing - review & editing. Philippe Dubois: Methodology; Supervision; Writing - review & editing. Przemysław Gorzelak: Conceptualization; Formal analysis; Funding acquisition; Investigation; Methodology; Project administration; Supervision; Visualization; Writing - review & editing.

References

1. D. J. Bottjer, E. H. Davidson, K. J. Peterson, R. A. Cameron, Paleogenomics of echinoderms, *Science* 314 (2006) 956–960.
2. H. U. Nissen, Crystal orientation and plate structure in echinoid skeletal units, *Science* 166 (1969) 1150–1152.

3. M.J. Simms, Stereom microstructure of columnal latera: a character for assessing phylogenetic relationships in articulate crinoids, *Swiss J. Palaeontol.* 130 (2011) 143–154.

4. A. B. Smith, Stereom microstructure of the echinoid test, *Spec. Pap. Palaeontol.* 25 (1980) 1–81.

5. D. B. Macurda, D. L. Meyer, The microstructure of the crinoid endoskeleton, *Univ. Kans. Paleontol. Contrib.* 74 (1975) 1–22.

6. T. Yang, Z. Jia, Z. Wu, *et al.* High strength and damage-tolerance in echinoderm stereom as a natural bicontinuous ceramic cellular solid. *Nat Commun* 13, 6083 (2022). https://doi.org/10.1038/s41467-022-33712-z

7. Ph. Dubois, M. Jangoux, Stereom morphogenesis and differentiation during regeneration of fractured adambulacral spines of *Asterias rubens* (Echinodermata, Asteroidea), *Zoomorphology* 109 (1990) 263–272.

8. P. Gorzelak, J. Stolarski, A. Dery, Ph. Dubois, S. Escrig, A. Meibom, Ultra- and micro-scale growth dynamics of the cidaroid spine of *Phyllacanthus imperialis* revealed by 26Mg labeling and NanoSIMS isotopic imaging, *J. Morphol.* 275(7) (2014) 788–796.

9. P. Gorzelak, J. Stolarski, P. Dubois, Ch. Kopp, A. Meibom, 26Mg labeling of the sea urchin regenerating spine: Insights into echinoderm biomineralization process, *J. Struct. Biol.* 176 (2011) 119–126.

10. B.M. Heatfield, D.F. Travis, Ultrastructural studies of regenerating spines of the sea urchin *Strongylocentrotus purpuratus* I. Cell types without spherules, *J. Morphol.* 145(1) (1975) 13–49.

11. P. Gorzelak, A. Dery, P. Dubois, J. Stolarski, Sea urchin growth dynamics at microstructural length scale revealed by Mn-labeling and cathodoluminescence imaging, *Front. Zool.* 14 (2017) 1–17.

12. S. Weiner, L. Addadi, Crystallization pathways in biomineralization, *Annu. Rev. Mater. Res.* 41 (2011) 21–40.
13. P. Dubois, L. Ameye, Regeneration of spines and pedicellariae in echinoderms: a review, *Microsc. Res. Tech.* 55(6) (2001) 427–437.
14. B. Schamberger, et al., Curvature in biological systems: Its quantification, emergence and implications across the scales, *Adv. Mater.* 35 (2023) 2206110.
15. B. Moreno, A. DiCorato, A. Park, K. Mobilia, R. Knapp, R. Bleher, C. Wilke, K. Alvares, D. Joester, Culture of and experiments with sea urchin embryo primary mesenchyme cells, *Methods Cell Biol.* 150 (2019) 293–330.
16. M.R. Winter, M. Morgulis, T. Gildor, A.R. Cohen, S. Ben-Tabou de-Leon, Calcium-vesicles perform active diffusion in the sea urchin embryo during larval biomineralization, *PLoS Comput. Biol.* 17(2) (2021) e1008780.
17. N.A. Stepicheva, M. Dumas, P. Kobi, J.G. Donaldson, J.L. Song, The small GTPase Arf6 regulates sea urchin morphogenesis, *Differentiation* 95 (2017) 31–43.
18. E. Hijaze, T. Gildor, R. Seidel, M. Layous, M. Winter, L. Bertinetti, Y. Politi, S. Ben-Tabou, S.B.T. de-Leon, ROCK and the actomyosin network control biomineral growth and morphology during sea urchin skeletogenesis, *Elife* 12 (2024) RP89080.
19. P. Vyas, C. Brannon, L. Formery, C.J. Lowe, M. Prakash, Algorithmic construction of topologically complex biomineral lattices via cellular syncytia, *bioRxiv* (2024) 2024.02.06.579287. https://doi.org/10.1101/2024.02.06.579287
20. T. Yang, H. Chen, Z. Jia, Z. Deng, L. Chen, E.M. Peterman, J.C. Weaver, L. Li, A damage-tolerant, dual-scale, single-crystalline microlattice in the knobby starfish, *Protoreaster nodosus*, *Science* 375(6581) (2022) 647–652.

21. P. Gorzelak, D. Kołbuk, J. Stolarski, P. Bącal, B. Januszewicz, P. Duda, D. Środek, T. Brachaniec, M.A. Salamon, A Devonian crinoid with a diamond microlattice, *Proc. R. Soc. B* 290(1995) (2023) 20230092.

22. A.L. Jessop, A.J. Millsteed, J.J. Kirkensgaard, J. Shaw, P.L. Clode, G.E. Schröder-Turk, Composite material in the sea urchin *Cidaris rugosa*: ordered and disordered micrometre-scale bicontinuous geometries, *J. R. Soc. Interface* 21(212) (2024) 20230597.

23. J. Feng, J. Fu, X. Yao, Y. He, Triply periodic minimal surface (TPMS) porous structures: from multi-scale design, precise additive manufacturing to multidisciplinary applications, *Int. J. Extrem. Manuf.* 4 (2022) 022001.

24. Z. Gan, M.D. Turner, M. Gu, Biomimetic gyroid nanostructures exceeding their natural origins. *Sci. Adv.* 2, (2016) e1600084(2016).DOI:10.1126/sciadv.1600084

25. S. Hyde, et al., *The Language of Shape*, Elsevier Science, 1996.

26. T.A. Del Valls, A.G. Dickson, The pH of buffers based on 2-amino-2-hydroxymethyl 1,3-propanediol ('tris') in synthetic sea water, *Deep-Sea Res. Part I* 45 (1998) 1541–1554.

27. C.A. Schneider, W.S. Rasband, K.W. Eliceiri KW. NIH Image to ImageJ: 25 years of image analysis, *Nature Methods* 2012, 9:671–675.

28. M. Morgulis, T. Gildor, M. Roopin, N. Sher, A. Malik, M. Lalzar, M. Dines, S. Ben-Tabou de-Leon, L. Khalaily, S. Ben-Tabou de-Leon, Possible cooption of a VEGF-driven tubulogenesis program for biomineralization in echinoderms, *Proc. Natl. Acad. Sci. U.S.A.* 116(25) (2019) 12353–12362.

29. R. Seidel, K. Handrich, M. Albéric, J. Perrin, D. Joester, Y. Politi, L. Bertinetti, Comparative structural analysis of stereom polymorphs in the sea urchin test, *Faraday Discussions*, 2025, 261, 340–358.

30. S. Ehrig, B. Schamberger, C. M. Bidan, A. West, C. Jacobi, K. Lam, P. Kollmannsberger,A. Petersen, P. Tomancak, K. Kommareddy, F. D. Fischer, P. Fratzl, J. W. C. Dunlop, Surface tensiondetermines tissue shape and growth kinetics. *Sci. Adv.* 5, eaav9394 (2019).

31. B. Tesson, M. Hildebrand, Dynamics of silica cell wall morphogenesis in the diatom *Cyclotella cryptica*: Substructure formation and the role of microfilaments, *J. Struct. Biol.* 169 (2010) 62–74.

32. G. Langer, L.J. De Nooijer, K. Oetjen, On the role of the cytoskeleton in coccolith morphogenesis: The effect of cytoskeleton inhibitors, *J. Phycol.* 46 (2010) 1252–1256.

33. G.M. Durak, C. Brownlee, G.L. Wheeler, The role of the cytoskeleton in biomineralisation in haptophyte algae, *Sci. Rep.* 7 (2017) 15409.

34. J. Tyszka, U. Bickmeyer, M. Raitzsch, J. Bijma, K. Kaczmarek, A. Mewes, M. Janse, Form and function of F-actin during biomineralization revealed from live experiments on foraminifera, *Proc. Natl. Acad. Sci. U.S.A.* 116(10) (2019) 4111–4116.